Mechanics Research Communications 42 (2012) 40–50

Contents lists available at SciVerse ScienceDirect

Mechanics Research Communications

journal homepage: www.elsevier.com/locate/mechrescom

A single strain-based growth law predicts concentric and eccentric cardiac growth during pressure and volume overload

Roy C.P. Kerckhoffs[a,*], Jeffrey H. Omens[b], Andrew D. McCulloch[a]

[a] Department of Bioengineering, Institute of Engineering in Medicine, University of California, San Diego, La Jolla, CA 92093-0412, USA
[b] Department of Medicine, Institute of Engineering in Medicine, University of California, San Diego, La Jolla, CA 92093-0412, USA

ARTICLE INFO

Article history:
Received 1 September 2011
Received in revised form
10 November 2011
Available online 22 November 2011

Keywords:
Cardiac growth
Remodeling
Overload
Computer model
Circulation
Ventricles

ABSTRACT

Adult cardiac muscle adapts to mechanical changes in the environment by growth and remodeling (G&R) via a variety of mechanisms. Hypertrophy develops when the heart is subjected to chronic mechanical overload. In ventricular pressure overload (e.g. due to aortic stenosis) the heart typically reacts by concentric hypertrophic growth, characterized by wall thickening due to myocyte radial growth when sarcomeres are added in parallel. In ventricular volume overload, an increase in filling pressure (e.g. due to mitral regurgitation) leads to eccentric hypertrophy as myocytes grow axially by adding sarcomeres in series leading to ventricular cavity enlargement that is typically accompanied by some wall thickening. The specific biomechanical stimuli that stimulate different modes of ventricular hypertrophy are still poorly understood. In a recent study, based on *in vitro* studies in micropatterned myocyte cell cultures subjected to stretch, we proposed that cardiac myocytes grow longer to maintain a preferred sarcomere length in response to increased fiber strain and grow thicker to maintain interfilament lattice spacing in response to increased cross-fiber strain. Here, we test whether this growth law is able to predict concentric and eccentric hypertrophy in response to aortic stenosis and mitral valve regurgitation, respectively, in a computational model of the adult canine heart coupled to a closed loop model of circulatory hemodynamics. A non-linear finite element model of the beating canine ventricles coupled to the circulation was used. After inducing valve alterations, the ventricles were allowed to adapt in shape in response to mechanical stimuli over time. The proposed growth law was able to reproduce major acute and chronic physiological responses (structural and functional) when integrated with comprehensive models of the pressure-overloaded and volume-overloaded canine heart, coupled to a closed-loop circulation. We conclude that strain-based biomechanical stimuli can drive cardiac growth, including wall thickening during pressure overload.

1. Introduction

Mature cardiac tissue adapts to mechanical changes in the environment via growth and remodeling (G&R) including hypertrophy (cell growth), fibrosis (formation of extra connective tissue), extracellular matrix (ECM) restructuring, necrosis (cell death) and apoptosis ("programmed" cell death) (Goktepe et al., 2010; Rosenkranz, 2004). Perhaps one of the best-known occurrences of cardiac G&R is the enlarged athlete's heart as a response to increased load. During exercise, large increases in cardiac output and heart rate are observed, but mean arterial pressure and end-diastolic pressure change very little (Zak, 1984). While the athlete's heart is considered to be a benign form of hypertrophy, ventricular hypertrophy in the pressure- or volume-overloaded heart ultimately becomes maladaptive. When the heart is subjected to chronic overload conditions, hypertrophy may be compensatory initially, but eventually leads to ventricular dysfunction and ultimately congestive heart failure. In ventricular pressure overload, the left ventricle experiences an increase in resistance as it ejects blood into the aorta (afterload increase). Common causes of LV pressure overload are systemic hypertension or aortic stenosis to which the ventricles typically react by concentric hypertrophic growth, characterized by thickening of the wall associated with cardiac cell thickening when sarcomeres – the cardiac cell's basic contractile units – are added in parallel (Gerdes, 1992). In volume overload, the heart experiences an increase in filling, or preload. Following ventricular volume overload – caused by for example a regurgitant mitral valve – eccentric hypertrophy ensues as cardiac cells grow axially by adding sarcomeres in series (Gerdes, 1992)

* Corresponding author at: University of California San Diego, Department of Bioengineering, 9500 Gilman Drive, La Jolla, CA 92093-0412, USA. Tel.: +1 858 822 4872; fax: +1 858 534 5722.
E-mail address: roy@eng.ucsd.edu (R.C.P. Kerckhoffs).

0093-6413/$ – see front matter © 2011 Elsevier Ltd. All rights reserved.
doi:10.1016/j.mechrescom.2011.11.004

leading to ventricular cavity enlargement that is typically accompanied by some wall thickening.

Biomechanical stimuli and neurohumoral factors are the two main triggers of cardiac G&R (Lorenz et al., 2009). Neurohumoral factors and their downstream signaling pathways that mediate cardiac hypertrophy are well known, but the specific biomechanical stimuli that stimulate different modes of ventricular hypertrophy are still poorly understood (Holmes, 2004; Lorenz et al., 2009; Omens, 1998). In the literature, various stimuli have been proposed including those that depend on: fiber strains at different stages in the cardiac cycle (Bupha-Intr et al., 2007; Guterl et al., 2007; Kroon et al., 2009); wall stress (Goktepe et al., 2010; Grossman et al., 1975); and regional strain-energy distributions (Vena et al., 2008). Of these, it has also been seen experimentally that hypertrophy and hypertrophic gene expression correlate better with strain than stress (Guterl et al., 2007; Omens, 1998). Strains have been proposed as stimuli for cardiac G&R as early as 1927 (Eyster et al., 1927). In cultured rat right ventricular papillary muscles, myocyte diameters increased independently of the level of stress with isometric contractions, whereas systolic shortening and/or diastolic lengthening regulated myocyte shape (Guterl et al., 2007). Grossman's original hypothesis that hypertrophy is compensatory, maintaining normal cardiac function by normalizing wall stress (Grossman et al., 1975), has been challenged in the last decade (Opie et al., 2006). For example, in genetically engineered mice it has been shown that despite inadequate normalization of wall stress, cardiac function showed little deterioration in pressure-overloaded animals with moderate hypertrophy responses (Esposito et al., 2002). In wild-type mice however with similar pressure overload, a significant increase in chamber dimensions and progressive deterioration in cardiac function occurred. In volume overloaded rats, Herrmann et al. (2003) found that stress remained chronically elevated but diastolic strains were normalized by an increase in myocardial stiffness associated with an increase in collagen crosslinks.

Micropatterned neonatal rat cardiac cell cultures restore resting sarcomere length when they are subjected to uniaxial static stretch (Mansour et al., 2004). Cells added about one sarcomere per hour after a 10% stretch in the fiber direction, thereby restoring resting sarcomere length and thus compensating for the stretch applied. When stretch is applied transversely to the fiber axis, immunofluorescent labeling of hypertrophic marker atrial natriuretic factor is increased, phosphorylation of focal adhesion kinase is increased and contractile protein synthesis is up regulated, as observed in pressure-overload (Gopalan et al., 2003; Russell et al., 2010; Simpson et al., 1999).

We have postulated in a previous study (Kerckhoffs, 2011) that cardiac cells would aim to maintain a preferred interfilament lattice spacing by adding sarcomeres in parallel in response to altered cellular cross-fiber strain. In support of this, Simpson et al. (1999) argued that an increase in cross-fiber strain during systolic loading is a critical signal for promoting myocyte hypertrophy during the evolution of concentric hypertrophy. In their experiments, cross-fiber stretch of aligned myocytes was most effective at promoting the accumulation of contractile proteins and branching myofibrils, phenotypic characteristics that are typically used to describe cardiac myocytes during concentric hypertrophy. This is in addition to the assumption that myocytes maintain sarcomere length during axial loading by series addition of sarcomeres. The proposed growth law – which included mechanisms for both axial and radial cellular growth – reproduced physiological postnatal growth to a substantial extent in a computational model of the rat left ventricle (Kerckhoffs, 2011). In the present study, the aim was to test whether a single growth law based on these principles is able to predict concentric or eccentric remodeling in response to aortic stenosis (pressure overload) or mitral valve regurgitation (volume overload), respectively, in an integrative computational model of the adult canine ventricles coupled to a closed-loop model of the circulation.

Table 1
Passive material properties.

Coefficient	Description	Value
C_{pas} [kPa]	Passive stress scaling constant	0.44
b_f	Parameter associated with fiber strain	18.5
b_t	Parameter associated with strain transmural to fiber and shear strain in radial-cross-fiber plane	3.58
b_{fr}	Parameter associated with shear strains in fiber-radial and fiber-crossfiber plane	1.63
C_{comp} [kPa]	Bulk modulus	350

2. Materials and methods

A non-linear finite element model of the beating canine right and left ventricles with realistic fiber anatomy was used in this study. The finite element model was coupled to a lumped-parameter model of the circulation that also included the heart valves. After modeling valve pathologies, the ventricles were allowed to adapt in shape in response to the mechanical stimuli, growing to a final state with a new geometry and hemodynamics.

2.1. Material properties

Passive material properties were described by a strain energy law W, consisting of the transversely isotropic version W_{pas} proposed by Guccione et al. (1991), and a slightly compressible part W_{comp} (Doll and Schweizerhof, 2000):

$$W = W_{pas} + W_{comp} \tag{1}$$

$$W_{pas} = \frac{1}{2} C_{pas}(e^{Q} - 1) \tag{2a}$$

$$Q = b_f E_{ff}^2 + b_t(E_{cc}^2 + E_{rr}^2 + 2E_{cr}^2) + b_{fr}(2E_{fc}^2 + 2E_{fr}^2) \tag{2b}$$

$$W_{comp} = \frac{C_{comp}(\det(\mathbf{F}) - 1)\ln(\det(\mathbf{F}))}{2} \tag{3}$$

E_{ff} is the Lagrangian strain in the fiber direction, E_{rr} is the transmural radial strain transverse to the fiber, E_{cc} is the cross-fiber strain perpendicular to the former two, and the remaining are associated shear strains. C_{pas}, C_{comp}, b_f, b_t, and b_{fr} are the material parameters (Table 1) and $\mathbf{F}$ is the deformation gradient tensor.

The contractile properties were described by a Hill-type model (Kerckhoffs et al., 2010; Lumens et al., 2009), that was modified so that active tension does not increase indefinitely with sarcomere length. This imposes a limit on the total amount of work a fiber can generate. See the online supplement for details.

2.2. Growth law

Growth was modeled by deforming the stress-free tissue configuration B_0 to a grown configuration B_g, which is not necessarily stress-free (Goktepe et al., 2010; Kroon et al., 2009; Rodriguez et al., 1994). The growth model is based on a multiplicative decomposition of the deformation gradient $\mathbf{F}$ first proposed by Rodriguez et al. (1994):

$$\mathbf{F} = \mathbf{F}_e \cdot \mathbf{F}_g \tag{4}$$

The growth deformation gradient $\mathbf{F}_g$ applies between B_0 and an intermediate fictitious configuration B'_g. The latter is a stress-free grown state where local kinematic compatibility conditions are not imposed. The deformation gradient $\mathbf{F}_e$ describes the deformation between B'_g and B_g and the Cauchy stress $\sigma(\mathbf{F}_e)$ in the tissue

only depends on this elastic deformation ($\mathbf{F}_g$ describes a plastic deformation).

2.2.1. Choice of biomechanical stimuli

The choice of biomechanical stimuli for cellular axial and radial growth were based on the following assumptions and experimental findings:

- Mechanical stimuli are local: individual cardiac cells remodel, hence the stimulus should be sensed by each myocyte. We make the assumption that cells deform similarly with the surrounding tissue as seen experimentally by Rodriguez et al. (1992).
- Strain-based stimuli correlate better with G&R than stress-based variables (Guterl et al., 2007; Omens, 1998);
- Stimuli should be independent of the hemodynamics of the cardiac cycle, in particular the timing of valve opening and closing: i.e. cells do not "know" when valves open and close. In the pressure-volume loop, end-systolic and end-diastolic states may be distinctive points in the cardiac cycle, but regionally cardiac phase changes are much more subtle (e.g. in stress–strain loops (Kerckhoffs et al., 2005, 2010)). Therefore, mechanical stimuli are likely to be found in extremes, amplitudes or means of strains (Holmes, 2004);
- *In vitro* experiments with isolated neonatal cardiac myocytes have demonstrated that cardiac myocytes are able to distinguish between strains applied in the fiber vs. cross-fiber direction (Gopalan et al., 2003; Mansour et al., 2004; Russell et al., 2010; Simpson et al., 1999);
- Because cells undergo cyclic motion, we assume that the time scale of a homeostatic set point is associated with the cardiac cycle duration, e.g. the stimulus for fiber axial growth could be the deviation from mean or maximum fiber strain, evaluated over a cardiac cycle. Naturally, the rate of hypertrophic response is much slower than a cardiac cycle, and thus many beats with supranormal fiber strain would be necessary to result in significant hypertrophy;
- All adaptation mechanisms should be present under all overload conditions. For example, fibers mostly grow axially in volume overload, which leads to eccentric hypertrophy, whereas fibers mostly grow radially in pressure overload, leading to concentric hypertrophy. But under pressure overload, the mechanism of fiber axial growth should also be active and vice versa, in volume overload, the mechanism of fiber radial growth should be active.

The above criteria led to the choice of a stimulus s_l for fiber axial growth driven by an imbalance in maximum fiber strain E_{ff} with a set-point $E_{ff,set}$ whereas fiber radial growth was driven by a stimulus s_t of imbalance in the smallest maximum principal strain in the cellular cross-sectional plane with a set point value:

$$s_l = \max(E_{ff}) - E_{ff,set} \tag{5}$$

$$s_t = \min(E_{cross,max}) - E_{cross,set} \tag{6}$$

in which $E_{cross,max}$ is the true algebraic maximum principal strain (not the maximum absolute magnitude) of the 2D cellular cross-sectional strain tensor E_{cross}:

$$E_{cross} = \begin{bmatrix} E_{cc} & E_{cr} \\ E_{cr} & E_{rr} \end{bmatrix} \tag{7}$$

where E_{cc}, E_{rr} and E_{cr} are the cross-fiber strain, radial strain and cross-fiber radial shear, respectively.

Both the maximum fiber strain and principal cross-sectional strains were evaluated over 1 cardiac beat.

Table 2
Growth properties.

Coefficient	Description	Value
$f_{ff,max}$ [1/day]	Maximum axial growth rate	0.3
f_f	Factor affecting slope of sigmoid for cellular axial growth	150
$s_{l,50}$	Stimulus value when 50% of maximum axial growth is reached	0.06
$F_{ff,50}$	Cumulative fiber growth stretch ratio when 50% of maximum fiber length is reached	1.35
$f_{length,slope}$	Factor affecting slope of axial growth evolution sigmoid	40
$f_{cc,max}$ [1/day]	Maximum radial growth rate	0.1
c_f	Factor affecting slope of sigmoid for cellular radial growth	75
$s_{t,50}$	Stimulus value when 50% of maximum radial growth is reached	0.07
$F_{cc,50}$	Cumulative fiber growth stretch ratio when 50% of maximum fiber thickness is reached	1.28
$c_{thickness,slope}$	Factor affecting slope of radial growth evolution sigmoid	60

All parameters, except $f_{ff,max}$ and $f_{cc,max}$, are dimensionless.

The cumulative growth deformation gradient tensor $\mathbf{F}_g^n$ was updated with the incremental growth deformation gradient tensor $\mathbf{F}_{g,i}$ (Kroon et al., 2009):

The deformation gradient tensors were defined with respect to the local fiber orientation ($\mathbf{F}_{ff}$ in fiber direction, $\mathbf{F}_{cc}$ cross-fiber parallel to the wall and $\mathbf{F}_{rr}$ radially), which allows for the definition of orthotropic (diagonal) cumulative and incremental growth tensors. The relation between components of $\mathbf{F}_{g,i}$ and the stimuli s_l and s_t were described by sigmoids:

$$\mathbf{F}_{g,i,ff} = \begin{cases} k_{ff}\dfrac{f_{ff,\max}\Delta t_{growth}}{1+\exp(-f_f(s_l - s_{l,50}))} + 1 & s_l \geq 0 \\ \dfrac{-f_{ff,\max}\Delta t_{growth}}{1+\exp(f_f(s_l + s_{l,50}))} + 1 & s_l < 0 \end{cases} \tag{8}$$

$$\mathbf{F}_{g,i,cc} = \begin{cases} \sqrt{k_{cc}\dfrac{f_{cc,\max}\Delta t_{growth}}{1+\exp(-c_f(s_t - s_{t,50}))} + 1} & s_t \geq 0 \\ \sqrt{\dfrac{-f_{cc,\max}\Delta t_{growth}}{1+\exp(c_f(s_t + s_{t,50}))} + 1} & s_t < 0 \end{cases} \tag{9}$$

$$\mathbf{F}_{g,i,rr} = \mathbf{F}_{g,i,cc} \tag{10}$$

Here, $\mathbf{F}_{g,i,ff}$ describes growth in the fiber direction due to the addition of sarcomeres in series at step i, whereas for $\mathbf{F}_{g,i,cc}$ and $\mathbf{F}_{g,i,rr}$ it is assumed that sarcomeres are added equally in parallel in both cross-fiber directions, hence transversely isotropic growth. Because material has to be deposited in two directions, the square root is taken of the growth stretch ratio in both cross-fiber directions. Δt_{growth} is the growth time step. For a description and values of the growth equation parameters, see Table 2. The relation between the incremental fiber axial growth $\mathbf{F}_{g,i,ff}$ and stimulus (Eq. (8)) contains a small quiescent region around the zero stimulus. Simpson et al. (1999) investigated protein metabolism in aligned myocytes stretched at varying degrees in the fiber and cross-fiber direction. A modest increase was observed in the total cellular concentration of myosin heavy chain and actin in cells stretched 2.5%. In Eq. (8), deviation of $\mathbf{F}_{g,i,ff}$ from ~0 occurs at 3% stretch above the set point (with 1% fiber axial growth per growth step). In experiments, cells responded to cross-fiber stretch as low as 0.5% (Simpson et al., 1999): hence, in our growth rule for fiber radial growth (Eqs. (9) and (10)), there is no distinct quiescent region, albeit growth is slower around a zero stimulus than at higher values.

The evolution growth functions k_{ff} and k_{cc} (Lubarda and Hoger, 2002) reduce the positive growth rates to zero when maximum cell length and thickness are reached (the latter two are quantified by

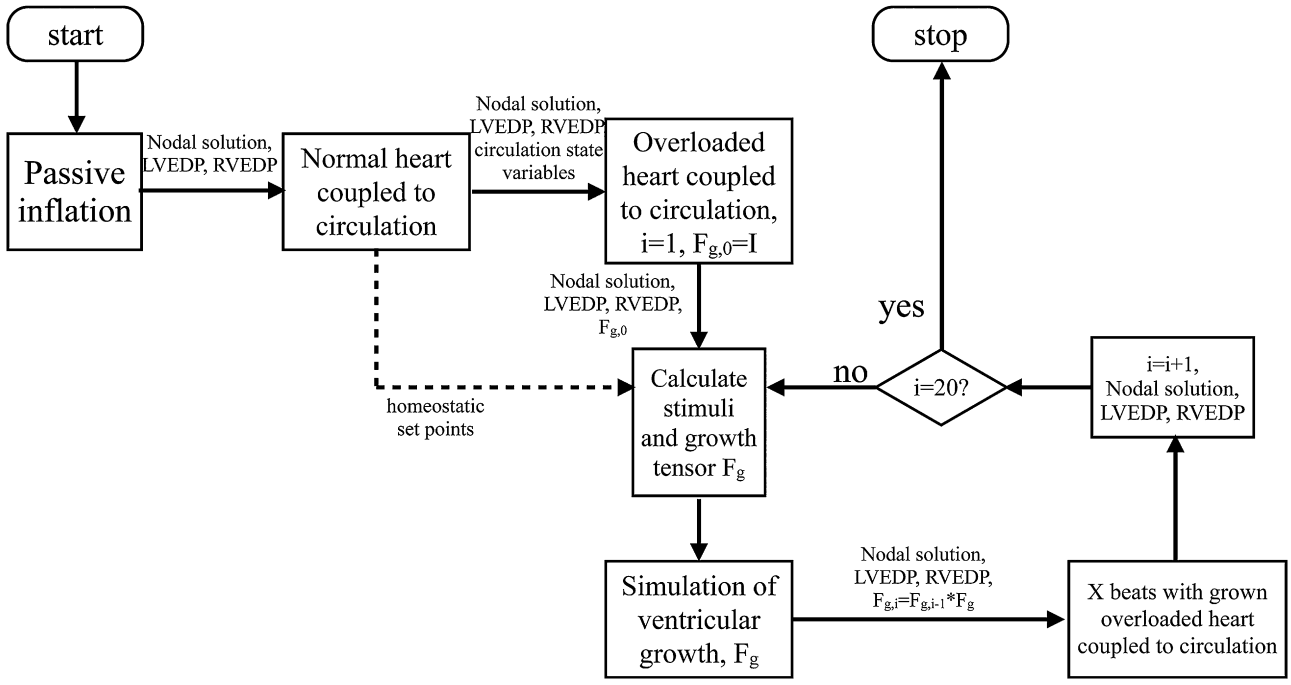

Fig. 1. Flow chart of the calculations performed. LVEDP, left ventricular end-diastolic pressure; RVEDP, right ventricular end-diastolic pressure; $\mathbf{F}_{g,i}$, cumulative growth tensor; $\mathbf{F}_g$, incremental growth tensor; $X = 5$.

the cumulative growth deformation tensor components $\mathbf{F}^i_{g,ff}$ and $\mathbf{F}^i_{g,cc}$, respectively, at step (i):

$$k_{ff} = \frac{1}{1 + \exp(f_{length,slope}(\mathbf{F}^i_{g,ff} - F_{ff,50}))} \tag{11}$$

$$k_{cc} = \frac{1}{1 + \exp(c_{thickness,slope}(\mathbf{F}^i_{g,cc} - F_{cc,50}))} \tag{12}$$

The parameter values ($f_{length,slope}$, $F_{ff,50}$, $c_{thickness,slope}$, $F_{cc,50}$) that characterize the growth evolution functions ensure a maximum cell axial growth ratio of about 1.54 (with a measured 200 μm maximum cell length, assuming a normal adult cell length of 130 μm)(Onodera et al., 1998) and a maximum cell radial growth ratio of 1.37 (with a measured 400 μm^2 maximum cell cross-sectional area, assuming a normal adult cell cross-sectional area of 215 μm^2)(Onodera et al., 1998). Note that the evolution growth functions are only used when the stimuli are positive: this will result in slow growth when maximum cell dimensions are being approached, but a normal shrink speed independent of cell dimensions.

2.3. Cardiovascular model

2.3.1. Normal heart

We have previously published a cardiovascular model of the normal canine heart, and employ that model here (Kerckhoffs et al., 2010). In brief, the model consisted of a 3D computational model that included the geometry and fiber architecture of the canine left and right ventricles, and coupling of the ventricular chambers to a closed circulation (Lumens et al., 2009). The latter was represented by a non-linear lumped parameter system model of the systemic and pulmonary circulation (the CircAdapt model (Arts et al., 2005)). The micro-adaptation algorithms of the CircAdapt model were not employed in this study. Peripheral resistance was adjusted to obtain the set cardiac output (1.8 l/min). For each beat, active tension generation was started synchronously with a basic cycle length of 750 ms.

All parameter values and initial conditions of the circulation models are listed in online supplement.

2.3.2. Pressure and volume overload models

The pressure overload model was represented by an aortic stenosis: this was achieved by changing the aortic valve opening area from 2.7 cm^2 in the normal state to 0.15 cm^2 in the diseased state. The volume overload model was represented by mitral regurgitation: this was achieved by changing the leaking area of the closed mitral valve from $5{\cdot}10^{-6}$ cm^2 in the normal state to 0.35 cm^2 in the diseased state. In both overload models, active tension generation was started synchronously for each beat with a basic cycle length of 600 ms (Nagatomo et al., 1999).

3. Calculation

3.1. Solution procedure

The FE anatomic model of the canine ventricles was discretized into 48 tricubic Hermite elements, with 1968 degrees of freedom. First, the left and right ventricles were inflated in 110 steps of 0.01 and 0.0018 kPa increments, respectively, to the initial end-diastolic pressures (decoupled from the circulatory model, see Fig. 1). At this point, the normal heart simulation was started without growth, fully coupled to the circulatory model, until reaching steady state (defined as relative difference in stroke volumes between LV and RV < 1%). For the last beat, maximum fiber strains and principal cross-sectional strains were recorded for all nodes. These values served as the set-points for the biomechanical stimuli in the overload simulations. The simulation was stopped at another end-diastolic state, which served as the new starting point for the overload simulations.

Next, the overload simulations were started without growth using the appropriate alterations for the valves, and were run to a new steady state at end-diastole. This phase represents the initial hemodynamically overloaded heart before hypertrophic growth.

At this point, the ventricles were allowed to grow. First, stimuli and the resulting growth tensors thereof were calculated from

the last (steady-state) cardiac cycle. Growth was introduced incrementally in the pressure- and volume-overloaded heart, decoupled from the circulation, at the last end-diastolic LV and RV pressures. Next, the simulation with the newly grown ventricles coupled to the circulation was restarted and continued for 5 cardiac cycles. This allowed the peripheral resistance to adjust to the new situation and to obtain a new acute steady-state. For the last of these 5 cardiac cycles, stimuli and growth tensors were again calculated and the procedure was repeated by inducing growth as mentioned earlier. A total of 20 growth steps were performed for both overload simulations. It should be emphasized that the parameter values of the aortic and mitral valve were the only differences between the two overload simulations.

After the simulations finished, unloaded geometries were obtained for each growth step by applying the calculated deformation growth tensors to the models' unloaded geometry.

3.2. Numerical implementation

The simulations were solved with Continuity 6.4b (http://www.continuity.ucsd.edu) in parallel using 12 processors, on a Linux cluster with dual Intel XeonX5650 6-core 2.66 GHz processors.

A time step of 1 ms was used for the simulations of the cardiac cycles, whereas a growth time step $\Delta t_{growth} = 1$ day was used for the growth simulations. However, this latter time step and its relation to the growth rate constants was later reassessed in comparison with experimental results. The nonlinear finite element models were solved with a modified Newton–Raphson iteration scheme. Integration was performed with $3 \times 3 \times 3$ Gaussian quadrature points. Convergence was reached when both the sum of incremental displacements and the sum of the residuals were lower than 10^{-5} mm and 10^{-8} N, respectively. The Jacobian was calculated and factorized in the first iteration of a new time step and when the solution was diverging. The system of linear equations was solved with SuperLU (Li and Demmel, 2003).

4. Results

4.1. Model validation of acute changes

Changes in global hemodynamics for the simulations of the overloaded hearts, compared with normal, were in good general agreement with experiments (Figs. 2 and 3, Table 3): end-diastolic pressures and volumes increased in the overloaded hearts, whereas forward ejection fraction decreased (22% and 30% during volume- and pressure-overload, respectively, vs. 48% in the normal heart). The volume-overloaded heart was characterized by the typical absence of isovolumic phases (Fig. 2) and a large total ejection fraction of 71% with a mitral regurgitant fraction of 61% (i.e. 61% of blood volume in the LV at end-diastole flows back into the left atrium during the next contraction). EDP however only doubled, whereas it tripled in dog experiments (Dell'Italia et al., 1995). Duration of ejection was shorter than in the normal heart. A peak cavity pressure of 218 mmHg characterized the pressure-overloaded heart and duration of ejection prolonged compared with the normal heart, which is also in agreement with experiments (Katz et al., 1928).

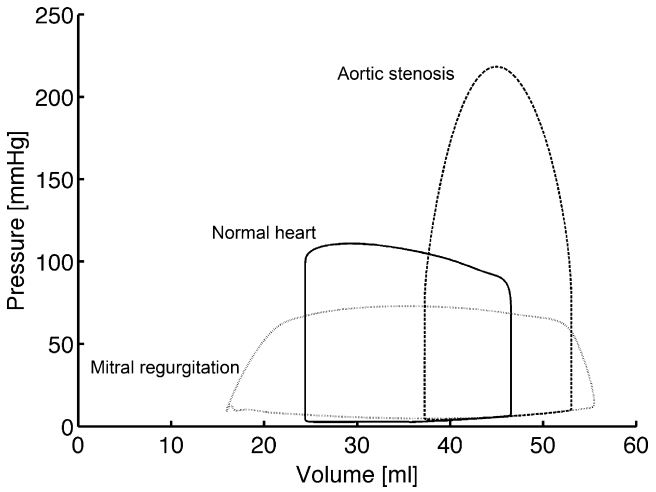

Fig. 2. Steady-state pressure-volume loops of the normal heart, acute aortic stenosis and acute mitral regurgitation simulations (before growth).

4.2. Model validation of chronic changes

4.2.1. Structure

In choosing a time to a growth step for the simulations, we compared the LV wall volume changes in our pressure-overload model with experimental values obtained at 5 days of aortic

Table 3
Acute hemodynamics (before growth) for the normal, pressure and volume overloaded hearts.

	Normal		Aortic stenosis		Mitral regurgitation	
	Simulation	Experiment	Simulation	Experiment	Simulation	Experiment
Heart rate [bpm]	80	87 ± 6 (Nagatomo et al., 1999)	100	104 ± 3 (Nagatomo et al., 1999)	100	111 ± 8 (Kihara et al., 1988)
dP/dt_{max} [mmHg/s]	2231	1627 ± 644 (Verbeek et al., 2003)	2466		1468	1200 ± 537 (Chen et al., 1991)
LVP_{max} [mmHg]	111	123 ± 7 (Nagatomo et al., 1999)	218	197 ± 5 (Nagatomo et al., 1999)	73	105 ± 28 (Chen et al., 1991)
LVEDP [mmHg]	6	6.4 ± 0.6 (Nagatomo et al., 1999)* 8 ± 5 (Dell'Italia et al., 1995)*	10	9.4 ± 0.7 (Nagatomo et al., 1999)*	12	23 ± 5 (Young et al., 1996)*(Dell'Italia et al., 1995)*
Systolic BP [mmHg]	111	122 ± 7 (Nagatomo et al., 1999)	90	68 ± 3 (Nagatomo et al., 1999)	73	
Diastolic BP [mmHg]	69	86 ± 5 (Nagatomo et al., 1999)	67	55 ± 2 (Nagatomo et al., 1999)	50	
Forward SV [ml]	22	26 ± 5 (Young et al., 1996) 44 ± 1.5 (Nagatomo et al., 1999)	16	40 ± 2 (Nagatomo et al., 1999)	12	
Mitral regurgitant fraction [%]	0		0		61	56 ± 18 (Dell'Italia et al., 1995)
Total LVEF [%]	48	47 ± 6 (Young et al., 1996) 38 (Verbeek et al., 2003)	30		71	

Experimental values are mean ± SD or mean ± SE, followed by literature references. BP, aortic blood pressure; LVEDP, left ventricular end-diastolic pressure; LVEF, left ventricular ejection fraction; LVP_{max}, peak LV cavity pressure; SV, stroke volume.

* Pulmonary artery wedge pressure instead of LVEDP.

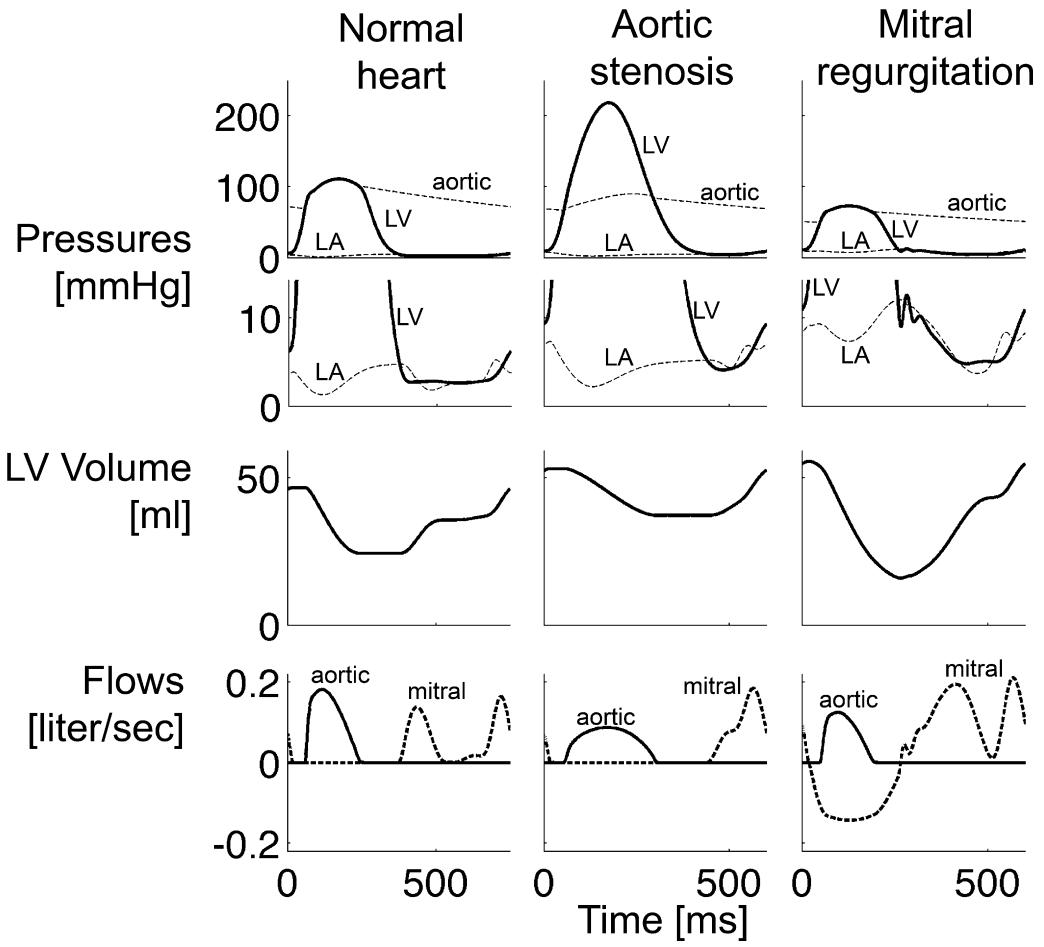

Fig. 3. Steady-state left atrial (LA), left ventricular (LV) and aortic pressures, LV volume, aortic and mitral flows of the normal heart, acute aortic stenosis and acute mitral regurgitation simulations (before growth).

stenosis in dog (Nagatomo et al., 1999). In this experiment, LV mass was increased by 11.1% at day 5. In our pressure-overload simulation, LV wall volume was increased by 9.8% and 13.3% at growth steps 3 and 4, respectively. Hence, one simulation growth step encompassed about 1.5 days. This means that with $\Delta t_{growth} = 1.5$ days, the maximum axial and radial growth rate constants $f_{ff,max}$ and $f_{cc,max}$ become 0.2 and 0.067 days^{-1}, respectively. Using this simple "time calibration" we further compared our results with those of experiments. With 20 growth steps, the total duration of growth encompassed about a month.

LV wall volume increased by 22% at day 10, which is similar to a 26.4% ($p < 0.05$) increase in LV mass in a canine pressure overload experiment after 10 days of aortic stenosis (Nagatomo et al., 1999) (Fig. 4). After about a month, LV wall volume in the model had increased by 42%. LV wall volume increased faster than LV cavity volume, exhibiting a concentric growth pattern, hence the LV wall volume to cavity volume decreased (Fig. 4, also for the RV). The LV in the pressure overload simulation also showed dilation: LV unloaded volume increased by 15% at day 10. LV dilation has also been demonstrated in a canine pressure overload experiment in which LV end-diastolic diameter increased by 4% ($p < 0.01$) after 9 days of aortic constriction (Sasayama et al., 1976). Even in reality, dilation appears to be a consistent factor in long-term G&R: for example, in the spontaneously hypertensive rat (SHR) fiber axial growth is a continuous process, surpassing fiber radial growth, leading to dilation in late stages of hypertrophy (Onodera et al., 1998).

In the pressure overload simulation, average LVFW wall thickness increased by 8% and 12% at day 10 and 20, respectively (Fig. 5),

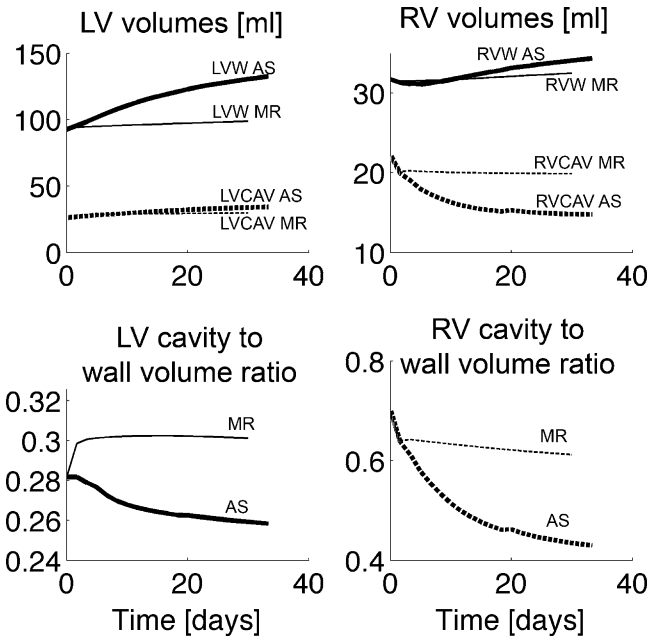

Fig. 4. Unloaded cavity and wall volume changes during growth for the pressure (thick lines) and volume overload simulations (thin lines). AS, aortic stenosis; MR, mitral regurgitation; LVW, left ventricular wall; LVCAV, left ventricular cavity; RVW, right ventricular wall; RVCAV, right ventricular cavity.

Table 4
Hemodynamics for the pressure and volume overloaded hearts.

	Aortic stenosis				Mitral regurgitation			
	Simulation (10 days)		Experiment (Nagatomo et al., 1999) (10 days)		Simulation (1 month)		Experiment (Young et al., 1996) (5–6 months)	
dP/dt_{max} [mmHg/s]	2155	(−13%)			1455	(−1%)		
LVP_{max} [mmHg]	221	(+1%)	212 ± 16	(+8%)	75	(0%)		
LVEDP [mmHg]	8.4	(−16%)	8.4*	(−10%)	10	(−16%)	15 ± 10*	(−35%)
Systolic BP [mmHg]	91	(+1%)	129 ± 9	(+90%)	75	(+2%)		
Diastolic BP [mmHg]	65	(0%)	89 ± 5	(+62%)	51	(+2%)		
Forward SV [ml]	15.9	(−1%)	34.6 ± 5	(−13.5%)	12	(−45%)#	21.5	(−19%)#
Mitral regurgitant fraction [%]	0				61		61 ± 15	
Total LVEF [%]	26	(−13%)			70	(+46%)#	56 ± 4	(+19%)#

Experimental values are mean ± SD or mean ± SE. Cells show absolute values and percentage change compared with the acute overload cases between parentheses, unless noted otherwise. BP, aortic blood pressure; LVEDP, left ventricular end-diastolic pressure; LVEF, left ventricular ejection fraction; LVP_{max}, peak LV cavity pressure; SV, stroke volume

* Pulmonary artery wedge pressure instead of LVEDP.

\# Compared with normal.

which is qualitatively similar to a 6% ($p < 0.001$) and 11% ($p < 0.0001$) increase in end-diastolic wall thickness in the aforementioned canine pressure overload experiment after 9 and 18 days of aortic constriction, respectively (Sasayama et al., 1976). The septum exhibited the largest average thickening (Fig. 5), whereas the RVFW thickened by 8% after a month.

In the volume overload simulation, dilation occurred rapidly early on (with the septum dilating the fastest), but slowed down at around the 5th day (Figs. 4 and 5). After a month, average cellular axial growth was 2%, 11% and −1% in the LVFW, septum and RVFW, respectively. Average wall thickening was 2% in the LVFW and 3% in the RVFW and septum.

After a month, LV wall volume increased by 7% and LV unloaded cavity volume by 14%, thus exhibiting an eccentric growth pattern (Fig. 4). In a volume overload experiment, LV mass increased by 19–27% after 5 months of mitral regurgitation (Dell'Italia et al., 1995; Young et al., 1996). RV wall volume increased by only 3%, comparable to experiments, in which RV mass was not significantly changed (Young et al., 1996). LV end-diastolic volume (LVEDV) increased by 37%, compared with the normal heart, whereas in a volume overload experiment, LVEDV increased by 74% after 5–6 months of mitral regurgitation (Young et al., 1996). The LV wall volume to cavity volume increased rapidly early on but stayed about constant thereafter (Fig. 4).

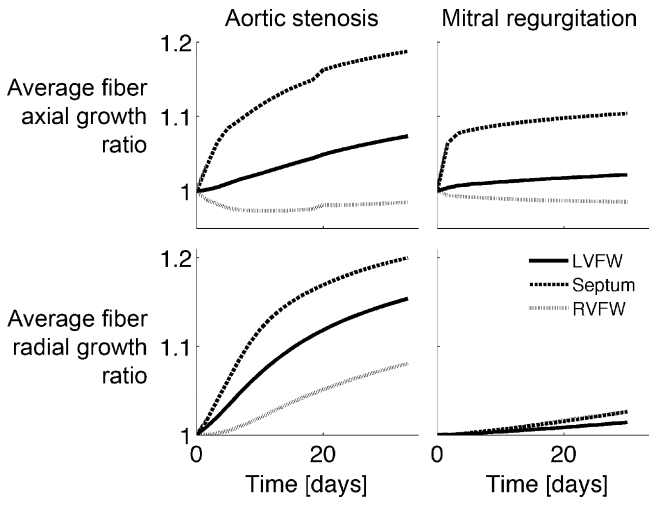

Fig. 5. Average growth stretch ratios in the left ventricular free wall (LVFW), right ventricular free wall (RVFW) and septum for the pressure (aortic stenosis) and volume overload simulations (mitral regurgitation).

4.2.2. Function

After 10 days, LVEDP decreased from 10 to 8 mmHg which is qualitatively similar to the −10% change in the canine pressure overload model after 10 days of aortic stenosis (Nagatomo et al., 1999) (Table 4). Large differences existed however in the blood pressures between simulation and experiment (Table 4).

In the volume overload model, dP/dt_{max} remained similar at 1455 mmHg/s. LVEDP and total ejection fraction decreased from 12 to 10 mmHg and from 71 to 70%. These changes are in good agreement with experiments (Dell'Italia et al., 1995; Young et al., 1996) (Table 4).

During systole, maximum cross-sectional principal strain decreased in the simulations of the normal heart. The same systolic downward trend of the maximum cross-sectional principal strain was observed in the simulation of aortic stenosis, but the magnitude of the peak negative strain in the pressure overload experiment was less than that in the normal heart (Fig. 6, right panel). Both strains reached a minimum during systole: the differences between these minima (between those from the aortic constriction simulation and the normal heart) are the stimuli for fiber radial growth. These strain courses are very similar to cross-fiber strains measured previously in the dog (Fig. 6, left panel).

5. Discussion

We have presented a strain-based cardiac growth law that includes fiber axial and radial cellular growth and tested it in whole heart simulations subjected to chronic pressure and volume overload. The main findings of this study were that: (1) a single growth law is able to reproduce most observed physiological responses, including both acute and chronic changes in structure and function, when integrated with two comprehensive computational models of the pressure-overloaded (by aortic stenosis) and volume-overloaded (by mitral regurgitation) canine heart, coupled to a closed-loop circulation and (2) a strain-based stimulus can drive wall thickening during pressure-overload as opposed to the more commonly proposed stress-based stimuli (Goktepe et al., 2010; Rausch et al., in press). This may reconcile previously contradictory in vivo and *in vitro* findings.

How do the biomechanical stimuli lead to the observed structural responses? Diastolic fiber strain – referred to the unloaded state – has previously been proposed and modeled as a stimulus for fiber axial growth (Arts et al., 2005; Emery and Omens, 1997; Goktepe et al., 2010; Omens, 1998). In addition, it has been shown experimentally that isolated cells grow axially in response to stretch applied parallel to their fiber axis (Mansour et al., 2004). Hence, during volume-overload (but also during

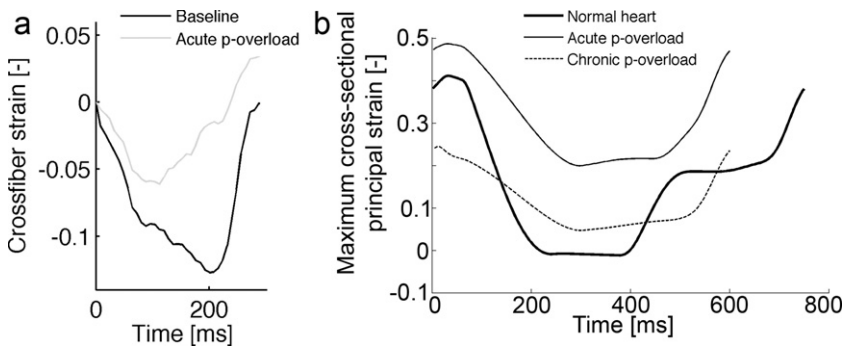

Fig. 6. LV midwall cross-fiber strains as a function of time for 1 cardiac cycle from a dog experiment, performed in our lab (left) (Howard et al., 2011) and maximum cross-sectional principal strain from current simulations (right). Activation is at zero ms. Cross-fiber strain decreases during systole in the normal heart (baseline) and during aortic constriction (acute p-overload), but the magnitude of the peak negative strain in the pressure overload experiment is less than that in the normal heart. Wall thickening through growth in the chronic pressure-overload simulation (right panel, after 18 growth steps) leads to normalization of the smallest strain value. Strain reference in the simulation was the unloaded state. Strain reference in the experiments was end-diastole and end-diastolic pressure for baseline and p-overload were matched.

pressure-overload), an increased preload increases end-diastolic volume and thus stretches fibers high enough above the set-points, triggering fiber axial growth throughout the LV myocardium. This leads to eccentric growth on the chamber level, since the fibers lie mostly in the plane of the ventricular wall. But fiber radial growth is likely regulated by a radially aligned structure: Russell et al. (2010) have suggested a possible mechanical cross-fiber strain sensor located at the Z-disc. Previously, we have presented a stimulus for fiber radial growth, based on the deviation of diastolic cross-fiber strain – also referred to the unloaded state – from zero (Kerckhoffs, 2011). This growth law was tested in a model of normal post-natal rat growth, loaded passively at end-diastole. To be able to test the growth law in a simulation of the beating heart, in the current study, the growth law was modified, such that fiber radial growth was induced by the deviation of the smallest maximum principal strain in the cellular cross-sectional plane. The largest difference with the previous study (Kerckhoffs, 2011) was the timing of the radial growth stimulus within the cardiac cycle (diastole vs. smallest value which occurs around end-systole). In a normal cardiac cycle at end-diastole, cells in the myocardium are stretched in the fiber direction and take on a more ellipsoidal cross-sectional shape (assuming unloaded fibers are circular in cross-section). In this short-axis cross-section, cells are compressed in cardiac radial direction (in the direction from endo- to epicardium) and stretched in the perpendicular direction (in-plane cross-fiber). The latter direction is closely aligned with the maximum principal cross-sectional strain. When cells are activated in systole, they shorten in the fiber direction, thicken radially and also shorten in cross-fiber direction (Fig. 6).

When the LV is subjected to an increased afterload, cells shorten and thicken less and cross-fiber strain remains higher than in the normal heart (Fig. 6). Taking the smallest value (of maximum cross-sectional principal strain) in the normal heart as a homeostatic set-point for fiber radial growth, the deviation from this value in the pressure overload simulation leads to a positive stimulus of fiber radial growth and tends to normalize cross-fiber strain back to the value in the normal heart (Fig. 6). This normalization occurs because the thicker fibers reach a lower maximum principal cross-sectional strain at end-diastole. Experimental evidence for this phenomenon however is still lacking.

The predictive power of the proposed multiscale model of cardiac mechanics and growth needs further testing. Experiments with ventricular pacing have shown acute redistribution of coronary perfusion and contraction (Prinzen et al., 1992; Waldman and Covell, 1987; Wyman et al., 1999): early in the cardiac cycle, myofibers shorten quickly against a low load in early-activated regions, while stretching fibers in late-activated regions. Later in the cycle, early-activated fibers are stretched whereas late-activated fibers contract against increased load. Long-term pacing leads to chronic asymmetric remodeling: the wall in early-activated regions become thinner whereas in late activated regions, the walls become thicker (Prinzen et al., 1995; van Oosterhout et al., 1998). The ability of the model to predict these measured regionally varying growth patterns would be a stringent test.

Although we make the assumption that a stimulus for cellular radial growth is associated with (1) a cellular cross-sectional strain and (2) that cross-fiber strain relates to interfilament lattice spacing change in vivo, there are other possible explanations of these mechanisms. With respect to the first point, several other stimuli candidates have been proposed in the literature (Holmes, 2004), including both stress and strain based growth laws. In a passive elastic tissue, one could achieve the equivalent results with either formulation. In the heart or other muscular tissues, it is theoretically possible to distinguish experimentally stress from strain during contraction. But we do not have sufficient knowledge of the molecular mechano-transductive complex of the myocyte to make this distinction. Most classical studies of ventricular hypertrophy have focused on systolic stress as a driver for concentric hypertrophy and diastolic stress (or strain) as the signal for eccentric hypertrophy (Grossman et al., 1975). But the results of in vivo experiments with genetically engineered mice and myocyte stretch studies have called these assumptions into question, as pointed out in the Introduction. With respect to the second point, ventricular deformation studies have shown that wall thickening during systole is dominated by interlaminar shearing (Costa et al., 1999; Legrice et al., 1995; Waldman et al., 1988). But since these studies measure strain at the tissue level, the contributions of cell cross-sectional shape change to wall thickening in vivo are not known.

Patient-specific modeling is the development of computational models of human pathophysiology that are individualized to patient-specific data with the goal to understand mechanisms of disease, monitor patients and evaluate treatment options specifically for a patient (Kerckhoffs, 2010; Neal and Kerckhoffs, 2010; Sachse and Seemann, 2009; Taylor and Figueroa, 2009; Trayanova, 2011). To date, virtually all patient-specific model results are evaluated acutely, thus ignoring chronic effects (for an exception, see (Lumens et al., 2010)). But validated comprehensive patient-specific models of cardiac (electro-) mechanics combined with growth and remodeling will become invaluable in predicting long-term effects of medical devices, surgeries and therapies on the heart. They will also provide a framework to gain an understanding of reverse remodeling mechanisms, for example in valve replacement/repair (Enriquez-Sarano et al., 1995; Webb et al., 2007), cardiac resynchronization therapy (Kass, 2005), cardiac restraint

device therapy (Acker, 2005; Klodell et al., 2008) and cardiac assist device therapy (Rogers et al., 2010; Trumble et al., 2011).

In the current study, we modeled the progression to *compensated* hypertrophy. In the future, the proposed models can serve as a framework for implementing increased mechanistic detail such as defective mechanotransduction pathways (Heineke and Molkentin, 2006). This will allow for in silico investigation of effects of altered remodeling pathways from the cell to the systems level on *decompensated* heart failure at multiple levels as well.

5.1. Limitations

5.1.1. Numerical implementation

Because of the large computational effort (each growth simulation requires about 3 weeks of computation time) it is not straightforward to perform a full-scale sensitivity analysis. However, a parameter variation analysis has been performed in our computational study of normal post-natal growth in the rat (Kerckhoffs, 2011). In the latter study, the ratio of the growth rate constants for fiber axial and radial growth was determined, such that normal post-natal growth of the LV radius and wall thickness matched those measured in experiments. This ratio has been replicated here in the parameters $f_{ff,max}$ and $f_{cc,max}$.

For the modeling of growth we followed the same approach as in Kroon et al. (2009) in which the ordinary differential equation for volume rate change is linearized with respect to the volume at the start of the growth increment. For other numerical schemes we refer the reader to Ambrosi et al. (2011).

5.1.2. Growth law

In the growth law, maximum cellular dimensions were limited by the growth evolution functions (Eqs. (11) and (12), but no limit was imposed on minimum dimensions. Cardiac myocytes may also have minimum dimensions, but these are unknown (Baskin and Taegtmeyer, 2011). Shrinking of myocytes however – which would be important in the modeling of reverse remodeling – does not play a role in the current study.

The results of a normal heart simulation were used to obtain the set points for the growth law, derived from the assumption that the normal ventricular model is at growth equilibrium prior to the hemodynamic overload. This approach makes the set points location-dependent, but all myocytes are possibly subjected to the same functional requirements. Hence, an interesting future study to consider is the simulation of a normal heart with uniform set points for fiber radial and axial growth. This will result in the development of residual stresses in the normal heart model (Kerckhoffs, 2011), which were also absent in the normal heart model in the current study.

5.1.3. Acute circulatory control

Overall, the acute changes (<1 min) in hemodynamics for the simulations of the overloaded hearts, compared with normal, were in good agreement with experiments. Peak LV cavity pressure in the volume-overload simulation however was lower than measured in experiments, which is most likely due to the absence of several fast baro-reflex responses in the models. For example, myocardial contractility was held constant throughout all simulations, but in reality increases due to beta-adrenergic stimulation when a drop in aortic pressure (or time-derivative thereof) is sensed by stretch-sensitive (baro-)receptors in the proximal aorta. Heart rate typically also increases. We prescribed a higher heart rate (from 80 to 100 bpm) as performed in canine pressure-overload experiments (Nagatomo et al., 1999). Increase in venous tone in order to increase venous return was another baro-reflex mechanism that was not included. We did include however the regulation of cardiac output by peripheral resistance which added to the increased preload in both overload simulations. Inclusion of these acute reflexes in future studies may result in a better starting point for the chronic growth simulations. For example, end-diastolic pressure in the acute volume-overload simulation remained rather low, compared with experiments, which led to a reduced stimulus for fiber axial growth and as a result, repressed dilation.

5.1.4. Long-term circulatory control

There are many other long-term adaptation mechanisms that were not included in the current study. For example, the atria in the heart (Kihara et al., 1988) and arteries and veins in the circulation also adapt their dimensions to altered hemodynamics (Arts et al., 2005). The absence of circulation adaptation may explain the discrepancy with experiments, observed in the blood pressures in the chronic pressure-overload simulation. A particular mechanism that was not included in the model is blood volume control, which in the CircAdapt model of the circulation is regulated by mean aortic pressure. In a preliminary simulation with variable blood volume, the volume-overload model exhibited much more physiological eccentric growth than in the present results. However, the pressure-overloaded heart also became exposed to a large preload and showed eccentric hypertrophy. Mean aortic pressure however is only one of many mechanisms of circulatory control. For example, there is an opposing mechanism of blood volume control by atrial stretch and ANP production, which was also not included in the model. Most likely, to achieve appropriate hypertrophy, a balance is needed between chronic and acute circulatory control on one side with ventricular growth laws on the other. Another possible explanation for the eccentric LV growth in response to blood volume change is that the fiber axial growth rate constant may have been too large: i.e. under pathological conditions, concentric hypertrophy seems to be a faster type of growth than eccentric (Moalic et al., 1981), whereas isolated myocytes show attenuated responses to stretch in the fiber direction compared with cross-fiber stretch (Simpson et al., 1999). Hence, further computational studies with long-term control mechanisms are needed in order to investigate these interactions between circulatory control and ventricular growth.

Other chronic changes currently not included that warrant future studies are changes in contractility, sensitivity to beta-adrenergic stimulation, fibrosis, extracellular matrix restructuring, necrosis and apoptosis.

Funding sources

The study has been supported by the National Biomedical Computation Resource (NIH grant P41 RR08605) (to A.D.M) and NIH grant R01 HL96544 (to A.D.M.). This investigation was conducted in part using a facility constructed with support from Research Facilities Improvement Program Grant Number C06 RR-017588-01 from the National Center for Research Resources, National Institutes of Health.

Acknowledgment

We thank Prof. Theo Arts for kindly providing the code for the CircAdapt model.

Appendix A. Supplementary data

Supplementary data associated with this article can be found, in the online version, at doi:10.1016/j.mechrescom.2011.11.004.

References

Acker, M.A., 2005. Clinical results with the acorn cardiac restraint device with and without mitral valve surgery. Semin. Thorac. Cardiovasc. Surg. 17, 361–363.

Ambrosi, D., Ateshian, G.A., Arruda, E.M., Cowin, S.C., Dumais, J., Goriely, A., Holzapfel, G.A., Humphrey, J.D., Kemkemer, R., Kuhl, E., Olberding, J.E., Taber, L.A., Garikipati, K., 2011. Perspectives on biological growth and remodeling. J. Mech. Phys. Solids 59, 863–883.

Arts, T., Delhaas, T., Bovendeerd, P., Verbeek, X., Prinzen, F.W., 2005. Adaptation to mechanical load determines shape and properties of heart and circulation: the CircAdapt model. Am. J. Physiol. Heart Circ. Physiol. 288, H1943–H1954.

Baskin, K.K., Taegtmeyer, H., 2011. Taking pressure off the heart: the ins and outs of atrophic remodelling. Cardiovasc. Res. 90, 243–250.

Bupha-Intr, T., Holmes, J.W., Janssen, P.M.L., 2007. Induction of hypertrophy in vitro by mechanical loading in adult rabbit myocardium. Am. J. Physiol. Heart Circ. Physiol. 293, H3759–H3767.

Chen, C., Rodriguez, L., Guerrero, J., Marshall, S., Levine, R., Weyman, A., Thomas, J., 1991. Noninvasive estimation of the instantaneous first derivative of left ventricular pressure using continuous-wave Doppler echocardiography. Circulation 83, 2101–2110.

Costa, K.D., Takayama, Y., McCulloch, A.D., Covell, J.W., 1999. Laminar fiber architecture and three-dimensional systolic mechanics in canine ventricular myocardium. Am. J. Physiol. Heart Circ. Physiol. 276, H595–H607.

Dell'Italia, L.J., Meng, Q.C., Balcells, E., Straeter-Knowlen, I.M., Hankes, G.H., Dillon, R., Cartee, R.E., Orr, R., Bishop, S.P., Oparil, S.<ET AL>, 1995. Increased ACE and chymase-like activity in cardiac tissue of dogs with chronic mitral regurgitation. Am. J. Physiol. Heart Circ. Physiol. 269, H2065–H2073.

Doll, S., Schweizerhof, K., 2000. On the development of volumetric strain energy functions. J. Appl. Mech. 67, 17–21.

Emery, J.L., Omens, J.H., 1997. Mechanical regulation of myocardial growth during volume-overload hypertrophy in the rat. Am. J. Physiol. Heart Circ. Physiol. 42, H1198–H1204.

Enriquez-Sarano, M., Schaff, H.V., Orszulak, T.A., Tajik, A.J., Bailey, K.R., Frye, R.L., 1995. Valve repair improves the outcome of surgery for mitral regurgitation: a multivariate analysis. Circulation 91, 1022–1028.

Esposito, G., Rapacciuolo, A., Naga Prasad, S.V., Takaoka, H., Thomas, S.A., Koch, W.J., Rockman, H.A., 2002. Genetic alterations that inhibit in vivo pressure-overload hypertrophy prevent cardiac dysfunction despite increased wall stress. Circulation 105, 85–92.

Eyster, J.A.E., Meek, W.J., Hodges, F.J., 1927. Cardiac changes subsequent to aortic lesions. Arch. Intern. Med. 39, 536–549.

Gerdes, A.M., 1992. The use of isolated myocytes to evaluate myocardial remodeling. Trends Cardiovasc. Med. 2, 152–155.

Goktepe, S., Abilez, O.J., Parker, K.K., Kuhl, E., 2010. A multiscale model for eccentric and concentric cardiac growth through sarcomerogenesis. J. Theor. Biol. 265, 433–442.

Gopalan, S.M., Flaim, C., Bhatia, S.N., Hoshijima, M., Knoell, R., Chien, K.R., Omens, J.H., McCulloch, A.D., 2003. Anisotropic stretch-induced hypertrophy in neonatal ventricular myocytes micropatterned on deformable elastomers. Biotechnol. Bioeng. 81, 578–587.

Grossman, W., Jones, D., McLaurin, L.P., 1975. Wall stress and patterns of hypertrophy in the human left ventricle. J. Clin. Invest. 56, 56–64.

Guccione, J.M., McCulloch, A.D., Waldman, L.K., 1991. Passive material properties of intact ventricular myocardium determined from a cylindrical model. J. Biomech. Eng. Trans. ASME 113, 42–55.

Guterl, K.A., Haggart, C.R., Janssen, P.M., Holmes, J.W., 2007. Isometric contraction induces rapid myocyte remodeling in cultured rat right ventricular papillary muscles. Am. J. Physiol. Heart Circ. Physiol. 293, H3707–H3712.

Heineke, J., Molkentin, J.D., 2006. Regulation of cardiac hypertrophy by intracellular signalling pathways. Nat. Rev. Mol. Cell. Biol. 7, 589–600.

Herrmann, K.L., McCulloch, A.D., Omens, J.H., 2003. Glycated collagen cross-linking alters cardiac mechanics in volume-overload hypertrophy. Am. J. Physiol. Heart Circ. Physiol. 284, H1277–H1284.

Holmes, J.W., 2004. Candidate mechanical stimuli for hypertrophy during volume overload. J. Appl. Physiol. 97, 1453–1460.

Howard, E.J., Covell, J.W., Mulligan, L.J., McCulloch, A.D., Omens, J.H., Kerckhoffs, R.C.P., 2011. Improvement in pump function with endocardial biventricular pacing increases with activation time at the left ventricular pacing site in failing canine hearts. Am. J. Physiol. Heart Circ. Physiol. 301, H1447–H1455.

Kass, D.A., 2005. Cardiac resynchronization therapy. J. Cardiovasc. Electrophysiol. 16, S35–S41.

Katz, L.N., Ralli, E.P., Cheer, S.-N., 1928. The cardiodynamic changes in the aorta and left ventricle due to stenosis of the aorta. J. Clin. Invest. 5, 205–227.

Kerckhoffs, R.C.P., 2010. Patient Specific Modeling of the Cardiovascular System: Technology-Driven Personalized Medicine. Springer, New York, NY, p. 265.

Kerckhoffs, R.C.P., 2011. Computational modeling of cardiac growth in the post-natal rat with a strain-based growth law. J. Biomech., doi:10.1016/j.jbiomech.2011.11.028.

Kerckhoffs, R.C.P., Faris, O., Bovendeerd, P.H.M., Prinzen, F.W., Smits, K., McVeigh, E.R., Arts, T., 2005. Electromechanics of paced left ventricle simulated by straightforward mathematical model: comparison with experiments. Am. J. Physiol. Heart Circ. Physiol. 289, H1889–H1897.

Kerckhoffs, R.C.P., Omens, J.H., McCulloch, A.D., Mulligan, L.J., 2010. Ventricular dilation and electrical dyssynchrony synergistically increase regional mechanical non-uniformity but not mechanical dyssynchrony: a computational model. Circ. Heart Fail. 3, 528–536.

Kihara, Y., Sasayama, S., Miyazaki, S., Onodera, T., Susawa, T., Nakamura, Y., Fujiwara, H., Kawai, C., 1988. Role of the left atrium in adaptation of the heart to chronic mitral regurgitation in conscious dogs. Circ. Res. 62, 543–553.

Klodell Jr., C.T., Aranda Jr., J.M., McGiffin, D.C., Rayburn, B.K., Sun, B., Abraham, W.T., Pae Jr., W.E., Boehmer, J.P., Klein, H., Huth, C., 2008. Worldwide surgical experience with the Paracor HeartNet cardiac restraint device. J. Thorac. Cardiovasc. Surg. 135, 188–195.

Kroon, W., Delhaas, T., Arts, T., Bovendeerd, P., 2009. Computational modeling of volumetric soft tissue growth: application to the cardiac left ventricle. Biomech. Model. Mechanobiol. 8, 301–309.

Legrice, I.J, Takayama, Y., Covell, J.W., 1995. Transverse-shear along myocardial cleavage planes provides a mechanism for normal systolic wall thickening. Circ. Res. 77, 182–193.

Li, X.S., Demmel, J.W., 2003. SuperLU_DIST: a scalable distributed-memory sparse direct solver for unsymmetric linear systems. ACM Trans. Math. Softw. 29, 110–140.

Lorenz, K., Schmitt, J.P., Vidal, M., Lohse, M.J., 2009. Cardiac hypertrophy: targeting Raf/MEK/ERK1/2-signaling. Int. J. Biochem. Cell Biol. 41, 2351–2355.

Lubarda, V.A., Hoger, A., 2002. On the mechanics of solids with a growing mass. Int. J. Solids Struct. 39, 4627–4664.

Lumens, J., Blanchard, D.G., Arts, T., Mahmud, E., Delhaas, T., 2010. Left ventricular underfilling and not septal bulging dominates abnormal left ventricular filling hemodynamics in chronic thromboembolic pulmonary hypertension. Am. J. Physiol. Heart Circ. Physiol. 299, H1083–H1091.

Lumens, J., Delhaas, T., Kirn, B., Arts, T., 2009. Three-wall segment (TriSeg) model describing mechanics and hemodynamics of ventricular interaction. Ann. Biomed. Eng. 37, 2234–2255.

Mansour, H., de Tombe, P.P., Samarel, A.M., Russell, B., 2004. Restoration of resting sarcomere length after uniaxial static strain is regulated by protein kinase C{epsilon} and focal adhesion kinase. Circ. Res. 94, 642–649.

Moalic, J.M., Bercovici, J., Swynghedauw, B., 1981. Protein synthesis during systolic and diastolic cardiac overloading in rats: a comparative study. Cardiovasc. Res. 15, 515–521.

Nagatomo, Y., Carabello, B.A., Hamawaki, M., Nemoto, S., Matsuo, T., McDermott, P.J., 1999. Translational mechanisms accelerate the rate of protein synthesis during canine pressure-overload hypertrophy. Am. J. Physiol. Heart Circ. Physiol. 277, H2176–H2184.

Neal, M.L., Kerckhoffs, R., 2010. Current progress in patient-specific modeling. Brief Bioinform. 11, 111–126.

Omens, J.H., 1998. Stress and strain as regulators of myocardial growth. Prog. Biophys. Mol. Biol. 69, 559–572.

Onodera, T., Tamura, T., Said, S., McCune, S.A., Gerdes, A.M., 1998. Maladaptive remodeling of cardiac myocyte shape begins long before failure in hypertension. Hypertension 32, 753–757.

Opie, L.H., Commerford, P.J., Gersh, B.J., Pfeffer, M.A., 2006. Controversies in ventricular remodeling. Lancet 367, 356–367.

Prinzen, F.W., Cheriex, E.C., Delhaas, T., Vanoosterhout, M.F.M., Wellens, H.J.J., Reneman, R.S., 1995. Asymmetric thickness of the left-ventricular wall resulting from asynchronous electric activation – a study in dogs with ventricular pacing and in patients with left-bundle-branch block. Am. Heart J. 130, 1045–1053.

Prinzen, F.W., Delhaas, T., Arts, T., Reneman, R.S., 1992. Effect of asynchronous electrical activation on regional contractile work in the canine left-ventricle. FASEB J. 6, A1232.

Rausch, M., Dam, A., Göktepe, S., Abilez, O., Kuhl, E. Computational modeling of growth: systemic and pulmonary hypertension in the heart. Biomech. Model. Mechanobiol., in press.

Rodriguez, E.K, Hoger, A., McCulloch, A.D., 1994. Stress-dependent finite growth in soft elastic tissues. J. Biomech. 27, 455–467.

Rodriguez, E.K., Hunter, W.C., Royce, M.J., Leppo, M.K., Douglas, A.S., Weisman, H.F., 1992. A method to reconstruct myocardial sarcomere lengths and orientations at transmural sites in beating canine hearts. Am. J. Physiol. Heart Circ. Physiol. 263, H293–H306.

Rogers, J.G., Aaronson, K.D., Boyle, A.J., Russell, S.D., Milano, C.A., Pagani, F.D., Edwards, B.S., Park, S., John, R., Conte, J.V., Farrar, D.J., Slaughter, M.S., 2010. Continuous flow left ventricular assist device improves functional capacity and quality of life of advanced heart failure patients. J. Am. Coll. Cardiol. 55, 1826–1834.

Rosenkranz, S., 2004. TGF-beta1 and angiotensin networking in cardiac remodeling. Cardiovasc. Res. 63, 423–432.

Russell, B., Curtis, M.W., Koshman, Y.E., Samarel, A.M., 2010. Mechanical stress-induced sarcomere assembly for cardiac muscle growth in length and width. J. Mol. Cell. Cardiol. 48, 817–823.

Sachse, F.B., Seemann, G., 2009. Special issue: functional imaging and modelling of the heart. Med. Image Anal. 13, 345.

Sasayama, S., Ross Jr., J., Franklin, D., Bloor, C., Bishop, S., Dilley, R., 1976. Adaptations of the left ventricle to chronic pressure overload. Circ. Res. 38, 172–178.

Simpson, D.G., Majeski, M., Borg, T.K., Terracio, L., 1999. Regulation of cardiac myocyte protein turnover and myofibrillar structure in vitro by specific directions of stretch. Circ. Res. 85, e59–e69.

Taylor, C.A., Figueroa, C.A., 2009. Patient-specific modeling of cardiovascular mechanics. Annu. Rev. Biomed. Eng. 11, 109–134.

Trayanova, N.A., 2011. Whole-heart modeling: applications to cardiac electrophysiology and electromechanics. Circ. Res. 108, 113–128.

Trumble, D.R., McGregor, W., Kerckhoffs, R.C.P., Waldman, L.K., 2011. Cardiac Assist with a twist: apical torsion as a means to improve failing heart function. J. Biomech. 133.

van Oosterhout, M.F.M., Prinzen, F.W., Arts, T., Schreuder, J.J., Vanagt, W.Y.R., Cleutjens, J.P.M., Reneman, R.S., 1998. Asynchronous electrical activation induces asymmetrical hypertrophy of the left ventricular wall. Circulation 98, 588–595.

Vena, P., Gastaldi, D., Socci, L., Pennati, G., 2008. An anisotropic model for tissue growth and remodeling during early development of cerebral aneurysms. Comput. Mater. Sci. 43, 565–577.

Verbeek, X., Vernooy, K., Peschar, M., Cornelussen, R.N.M., Prinzen, F.W., 2003. Intra-ventricular resynchronization for optimal left ventricular function during pacing in experimental left bundle branch block. J. Am. Coll. Cardiol. 42, 558–567.

Waldman, L.K., Covell, J.W., 1987. Effects of ventricular pacing on finite deformation in canine left-ventricles. Am. J. Physiol. 252, H1023–H1030.

Waldman, L.K., Nosan, D., Villarreal, F., Covell, J.W., 1988. Relation between transmural deformation and local myofiber direction in canine left-ventricle. Circ. Res. 63, 550–562.

Webb, J.G., Pasupati, S., Humphries, K., Thompson, C., Altwegg, L., Moss, R., Sinhal, A., Carere, R.G., Munt, B., Ricci, D., Ye, J., Cheung, A., Lichtenstein, S.V., 2007. Percutaneous transarterial aortic valve replacement in selected high-risk patients with aortic stenosis. Circulation 116, 755–763.

Wyman, B.T., Hunter, W.C., Prinzen, F.W., McVeigh, E., 1999. Mapping propagation of mechanical activation in the paced heart with MRI tagging. Am. J. Physiol. Heart Circ. Physiol. 276, H881–H891.

Young, A.A., Orr, R., Smaill, B.H., Dell'Italia, L.J., 1996. Three-dimensional changes in left and right ventricular geometry in chronic mitral regurgitation. Am. J. Physiol. 271, H2689–H2700.

Zak, R., 1984. Growth of the Heart in Health and Disease. Raven Press, New York.